Progress In Electromagnetics Research B, Vol. 48, 197–220, 2013

NEAR-FIELD ERROR ANALYSIS FOR ARBITRARY SCANNING GRIDS USING FAST IRREGULAR ANTENNA FIELD TRANSFORMATION ALGORITHM

Muhammad A. Qureshi*, Carsten H. Schmidt, and Thomas F. Eibert

Technische Universität München, Lehrstuhl für Hochfrequenztechnik, Munich 80290, Germany

Abstract—An extensive error analysis for arbitrary near-field antenna measurements is performed. Expressions are derived to estimate the far-field uncertainty using the available near-field data together with the measurement inaccuracy but, most importantly, without the knowledge of the reference far field. Error analysis techniques presented so far either assume a specific set of antennas or a specific measurement surface and are difficult to generalize. We present a generalized approach providing realistic error estimates using the recently developed Fast Irregular Antenna Field Transformation Algorithm (FIAFTA). FIAFTA utilizes equivalent plane wave sources to represent radiated antenna fields and is able to process near-field data collected on arbitrary measurement grids. The unknown plane wave coefficients are determined by solving a linear system of equations. The error model is applied to planar, cylindrical, and spherical near-field measurements and is also valid for arbitrary measurement grids. The estimated far-field uncertainties show good agreement with the reference far-field errors.

1. INTRODUCTION

Near-field antenna measurements in combination with near-field far-field transformations constitute an effective way to determine the radiation characteristics of an antenna under test (AUT) [1]. The approach provides a good alternative to space limited direct far-field measurements and expensive compact ranges for large antennas, but at the cost of great care required during the near-field measurements.

Received 15 December 2012, Accepted 25 January 2013, Scheduled 27 January 2013

* Corresponding author: Muhammad Ayyaz Qureshi (ayyaz.qureshi@mytum.de).

No matter what precautions are used, there will always be several measurement and environmental errors in a practical setup. Therefore, a reliable error estimate in the far field against inaccuracies in the near field is one of the primary concerns. Several attempts have been made in the past and a well established body of literature is already available but either for some specific scanning geometries or for a specific set of antennas.

A major computer simulation based study for planar near-field measurement errors has been performed by Rodrigue et al. in [2]. Rodrigue perturbed the hypothetical near field with position and instrumentation errors to determine the far-field behavior. Newell and Crawford estimated the scan area truncation error [3] by utilizing the measured near-field data. The first specific error analysis for planar near-field antenna measurements has been performed by Yaghjian [4] to determine upper bound errors in far-field parameters. With a rigorous theoretical analysis, he derived expressions for estimating the uncertainty in the far field due to scan area truncation, probe positioning inaccuracies, instrumentation errors, and multiple reflection errors. However, the analysis is only valid for electrically large antennas ($> 10\lambda$) and it is assumed that the size of the scan plane is appreciably larger than the antenna size. Also, for the probe position inaccuracy, the worst case error is assumed in the direction of observation involving the side lobe region. A similar concept is valid for other errors as well. Therefore, the resulting error estimates predict an error which is unrealistically high. Newell performed more realistic error analyses in [5] making use of a known spatial dependency of the errors. This comprehensive analysis identifies the significant errors and also estimates the magnitude of all near-field error sources. The presented 18-term error model in [5] is formally accepted by the National Institute of Standards (NIST) (formerly called National Bureau of Standards). Error equations are derived to determine the relationship between the measurement errors and the far-field results. However, the analysis is again valid only for planar scanning surfaces and assumes antennas with electrical size $> 4\lambda$ for the derivation of the error equations. A more rigorous methodology is presented in [6] for the accuracy qualification of near-field measurement ranges. The methodology involves computer simulation, component certification, self tests, and comparison tests to determine upper bound far-field errors due to near-field measurement errors. Afterwards a near-field error budget is proposed for each near-field system component.

A detailed error analysis for spherical near-field measurements is presented in [7]. Mechanical inaccuracies, spherical area truncation, receiver errors, probe parameter errors etc. are considered and the

results of computer simulations with known inaccuracies are compared with inaccuracies in real measurements. The emphasis of the analysis is mainly on errors occurring in the main beam and in the first side lobe region. Nevertheless, it is stated that the results are applicable only for directive spot-beam antennas and may only be considered as guidelines. There are many other contributions in which authors address individual error sources and in some cases also propose error correction techniques. The error studies include, e.g., probe positioning error compensation [8–10], effect of random errors [11], reduction of measurement area truncation error [12, 13], analysis of system phase errors [14], methods to reduce leakage errors [15], etc..

A common observation implicit in the available literature is that either the error analysis is performed only for a given set of antennas or it assumes a specific scanning geometry. Error equations are not generalized and may not be applicable to all antennas. Also, the analysis is usually performed with emphasis on estimating the error in the main beam and in the first side lobe of the transformed far field. Estimating the mean and the maximum errors within the entire valid angle of the transformed far field requires a more rigorous analysis. It is highly desirable to develop an error model which is suitable for arbitrary measurement grids and is suitable for all kinds of antennas. The error model should also provide realistic error estimates and should not always consider the worst case scenario.

In this contribution, we present an extensive error analysis for arbitrary near-field measurements valid for all kinds of antennas. The analysis is based on the recently proposed Fast Irregular Antenna Field Transformation Algorithm (FIAFTA) [16, 17] which makes use of equivalent plane wave sources for representing the radiated AUT fields. The sole algorithm is capable of processing near-field data collected on standard as well as arbitrary measurement grids with full probe correction. A linear system of equations is formulated to determine the unknown plane wave coefficients. The linearity of the forward operator makes it possible to oversee the effect of near-field errors and to estimate the mean and the maximum error in the transformed far field. The accuracy of the estimated uncertainty in the far field is dependent on the knowledge of the near-field measurement inaccuracies. The magnitude of the near-field measurement errors is usually available for the near-field measurement ranges, e.g., the corrected planarity (RMS) of a planar NSI scanner 300 V-6 $\times$ 6 is 0.025 mm [18]. Also, the uncertainty in the received near-field magnitude via Rohde & Schwarz vector network analyzers R & S ®ZVL for 6–13.6 GHz frequency range is < 0.2 dB for pattern levels from 0 dB to -50 dB [19]. Similarly, the magnitude of other near-field

measurement inaccuracies can be extracted from the data sheets of the equipment. Once the uncertainties in near-field parameters are known, they can be used to find the uncertainty in the plane wave spectrum representing the AUT fields and hence the error in the far field. The error behavior of FIAFTA against planar near-field measurement errors in comparison with the traditional technique employing the two dimensional Fast Fourier Transform (2D FFT) has already been performed. FIAFTA is found more stable against scan area truncation errors [20], instrumentation errors [21], and probe pattern inaccuracies [22, 23], while other errors have a similar effect on both techniques.

Section 2 revisits the essentials of FIAFTA. In Section 3, an error analysis for arbitrary measurement grids is performed after dividing the error sources into five categories. The performance of the proposed error model is evaluated by introducing errors in the near-field data of synthetically modeled horn antennas. Section 4 concludes and summarizes the paper.

2. FAST IRREGULAR ANTENNA FIELD TRANSFORMATION ALGORITHM

FIAFTA is a plane wave based approach which utilizes plane waves as equivalent sources to represent the radiated AUT fields. Unlike other plane wave based approaches, FIAFTA considers the distribution of plane wave sources in all spatial directions. FIAFTA is valid for all kinds of antennas and is able to process the near-field data collected on an arbitrary grid. Furthermore, full probe correction without increase in numerical complexity makes FIAFTA an attractive choice. It should be mentioned here that the given error analysis is equally valid for other near-field far-field transformation techniques making use of equivalent sources but we chose FIAFTA due to its lower computational burden for arbitrary measurement grids and probes. In the following, we describe the essentials of FIAFTA.

The near-field probe takes the weighted average of the field around a measurement point according to the receiving characteristics and the output signal

$$U\left(\mathbf{r}_{\mathrm{M}}\right) = \iiint\limits_{V_{\mathrm{probe}}} \mathbf{w}_{\mathrm{probe}}\left(\mathbf{r}\right) \cdot \ \mathbf{E}\left(\mathbf{r}\right) dV \tag{1}$$

is acquired at the measurement point $\mathbf{r}_{\mathrm{M}}$. V_{probe} is the volume of the probe and $\mathbf{w}_{\mathrm{probe}}$ is the spatial weighting function of the probe. FIAFTA relates the plane wave spectrum and the near-field samples using the diagonal translation operator $T_L(\hat{k}, \mathbf{r}_{\mathrm{M}})$ (known from the Fast

Multipole Method [24]) according to

$$U(\mathbf{r}_{\mathrm{M}}) = -\mathrm{j}\frac{\omega\mu}{4\pi}\iint T_L\left(\hat{k},\mathbf{r}_{\mathrm{M}}\right)\bar{\mathbf{P}}\left(\hat{k},\hat{r}_{\mathrm{M}}\right)\cdot\left(\bar{\mathbf{I}}-\hat{k}\hat{k}\right)\cdot\tilde{\mathbf{J}}\left(\hat{k}\right)d\hat{k}^2, \quad (2)$$

where $\bar{\mathbf{P}}(\hat{k},\hat{r}_{\mathrm{M}})$ contains the far-field pattern of the probe for probe correction and $(\bar{\mathbf{I}}-\hat{k}\hat{k})\cdot\tilde{\mathbf{J}}(\hat{k})$ are the equivalent plane wave sources. The diagonal translation operator simply translates the propagating plane waves from the AUT to incident plane waves at the observation point $\mathbf{r}_{\mathrm{M}}$ as

$$T_L\left(\hat{k},\mathbf{r}_{\mathrm{M}}\right) = -\mathrm{j}\frac{k}{4\pi}\sum_{l=0}^{L}(-\mathrm{j})^l\,(2l+1)\,\mathrm{h}_l^{(2)}\left(k\mathbf{r}_{\mathrm{M}}\right)\mathrm{P}_l\left(\hat{k}\cdot\hat{r_{\mathrm{M}}}\right), \quad (3)$$

where $\mathrm{h}_l^{(2)}$ is the spherical Hankel function of second kind and P_l is the Legendre polynomial. The multipole order L for the diagonal translation operator is dependent on the size of the AUT and the size of the probe [25]. Two orthogonal polarizations of the radiated AUT field are commonly required. Therefore, two complex voltages are introduced and the spectral integral over the Ewald sphere is evaluated by numerical quadrature [24] with discrete representation according to

$$\begin{aligned} U^{1/2}\left(\phi_m,\theta_n,r_{\mathrm{M}}\right) \;=\; & -\mathrm{j}\frac{\omega\mu}{4\pi}\sum_{k_\phi}\sum_{k_\theta}T_L(\hat{k},\mathbf{r}_{\mathrm{M}})W(k_\theta) \\ & \mathbf{P}^{1/2}\left(k_\phi,k_\theta,\phi_m,\theta_n\right)\cdot\left(\bar{\mathbf{I}}-\hat{k}\hat{k}\right)\cdot\tilde{\mathbf{J}}\left(k_\phi,k_\theta\right), \quad (4) \end{aligned}$$

where $W(k_\theta)$ is a weighting factor for numerical quadrature and $m = 1,\ldots,M$ and $n = 1,\ldots,N$ denote the number of observation points in ϕ- and θ-direction, respectively. For enhanced computational complexity, near-field measurement points are grouped together to form a hierarchical structure similar to the Multilevel Fast Multipole Method (MLFMM) [26] as described in [17].

3. NEAR-FIELD ERROR ANALYSIS

The error behavior of FIAFTA is analyzed by developing a linear system of equations

$$\mathbf{U}' = -\mathrm{j}\frac{\omega\mu}{4\pi}\left\|C\right\|\cdot\tilde{\mathbf{J}}' \quad (5)$$

using (4), where $\mathbf{U}'$ is a vector containing the probe output for all measurement points and $\tilde{\mathbf{J}}'$ contains the plane wave coefficients of the AUT. The diagonal translation operator $T_L(\hat{k},\mathbf{r}_{\mathrm{M}})$, the weighting factor $W(k_\theta)$, and the probe correction coefficient $\bar{\mathbf{P}}(\hat{k},\hat{r}_{\mathrm{M}})$ are

combined to form the coupling matrix $\|C\|$. The given set of linear equations is solved using the Generalized Minimum Residual Solver (GMRES) [27] in a least mean square sense (LMS) [28] as

$$\|C\|^H \mathbf{U}' = -\mathrm{j}\frac{\omega\mu}{4\pi} \|C\|^H \|C\| \tilde{\mathbf{J}}', \tag{6}$$

where $\|C\|^H$ is the complex conjugate transpose of the coupling matrix. Near-field errors are divided into five major categories based on their influence on the probe output, probe correction coefficient, and the translation operator. The other two categories include computational errors due to inappropriate selection of parameters during the transformation and miscellaneous errors like aliasing errors, scan area truncation, etc..

The AUT used in the error analysis is synthetically modeled and electric dipoles are used to model the AUT with proper magnitude profile and geometrical arrangement as explained in [29]. It must be emphasized here that the analysis itself is equally valid for practical measurements. The only reason for using the synthetic approach is to compare the estimated errors with that of the observed errors in reference to the ideal far field. Also, the effect of each near-field error on the transformed far field can be isolated. A medium gain horn ($4\,\lambda$) is designed with source dipoles arranged in concentric circles. The accumulative effect of all the source dipoles determines the electric field

$$\mathbf{E}\left(\mathbf{r}_\mathrm{M}\right) = -\mathrm{j}\frac{\omega\mu}{4\pi} \sum_{i=1}^{i_\mathrm{AUT}} \left(\bar{\mathbf{I}} + \frac{1}{k^2}\nabla\nabla\right) \cdot \mathbf{d}_i \frac{\mathrm{e}^{-\mathrm{j}k\left|\mathbf{r}_\mathrm{M}-\mathbf{r}_{\mathrm{d},i}\right|}}{\left|\mathbf{r}_\mathrm{M}-\mathbf{r}_{\mathrm{d},i}\right|} \tag{7}$$

at the measurement point $\mathbf{r}_\mathrm{M}$ by evaluating the Green's function of free space, where $\mathbf{r}_{\mathrm{d},i}$ represents the source dipole positions, ω is the angular frequency, k is the wavenumber of free space, $\bar{\mathbf{I}}$ is the unit dyad, and $\mathbf{d}_i$ represents the amplitude, phase, and polarization information of the source dipoles. The near-field data and the ideal far field used in the analysis are computed using (7).

3.1. Computational Errors

It is conventionally assumed that the errors due to theoretical approximations are negligible. However, there are various parameters involved in the formulation of FIAFTA which determine the accuracy of the transformed far-field. A careful selection of these parameters is necessary in order to assume negligible errors in the transformed far field. We will discuss major factors here along with their effect on the transformed results.

3.1.1. Number of Levels and Buffer Boxes

There are factors like the number of levels in the multilevel approach[†] and the number of buffer boxes [30] which affect the transformed pattern. The number of levels is chosen keeping in view the size of the AUT and the probe. The optimum choice of the number of levels varies from case to case, e.g., for planar scanning surfaces a cubical box structure with minimum box size chosen according to the size of the probe and maximum box size chosen according to the minimum separation between the AUT and the probe gives the optimum results. If the hierarchical structure is not chosen properly, the multilevel approach might even result in consuming more time instead of improving the computational time. The effect on the accuracy, however, remains negligible. The buffer boxes are used to maintain a certain distance between the minimum spheres enclosing the AUT and the probe. The minimum spheres must not overlap in order for the representation to converge. For a good accuracy a larger separation between the AUT and the probe is recommended and is achieved by increasing the number of buffer boxes.

3.1.2. Multipole Order of AUT and T_L

The multipole order used to compute the translation operator effects the accuracy of FIAFTA. A semi-empirical formula to compute the multipole order L_{T_L} [25] is

$$L_{T_L} = kd/2 + 1.8d_o^{2/3}(kd)^{1/3}, \tag{8}$$

where $d = d_{\mathrm{a}} + d_{\mathrm{p}}$ is the sum of diameters of the smallest spheres enclosing the AUT and the probe antenna, respectively, while $d_o = \log(1/\gamma)$ is the factor controlling the desired accuracy of the expansion. In a similar fashion, the AUT multipole order is approximated as [7]

$$L_{\mathrm{AUT}} \simeq kd_{\mathrm{a}}/2 + 10. \tag{9}$$

The translation operator incorporates the effect of both the probe and the AUT and requires larger spectral content. Therefore, the multipole order of the translation operator is larger than the multipole order of the AUT. The accuracy of the multipole expansion is controlled by γ, i.e., choosing a very low value of γ, results in insufficient spectral content for accurate representation of the radiation pattern. On the other hand, very high values make the second order Hankel

[†] In the multilevel approach the computational complexity is reduced from $O((ka)^4)$ to $O((ka)^2\log(ka)^2)$ by grouping measurement points in a hierarchical fashion. Translations are then performed on the coarsest level and are processed through various levels until the observation point is reached (see [17] for more details).

function $\mathrm{h}_l^{(2)}(kr_\mathrm{M})$ to approach infinity quickly and thus deteriorate the resulting pattern. The maximum error level observed in the transformed field of the horn antenna operating at 10 GHz against a varying multipole order and considering 3 buffer boxes is shown in Fig. 1.

Similar analyses were carried out for a variety of antennas (electrical size varying from 4λ to 64λ) and the empirically deduced value of γ is found to be $\simeq 10^{-4}$. The observed maximum error level for the same value of γ for a horn antenna is ≤ -90 dB in both E and H plane pattern cuts (see Fig. 1 for multipole order = 24).

3.1.3. Residuum of GMRES Solver

As already stated, FIAFTA is implemented in an iterative fashion using a GMRES solver. The optimum selection of the relative residuum

$$r = \frac{\mathrm{norm}\left(\|C\|^H \|C\| \tilde{\mathbf{J}}'_{\mathrm{final}} - \|C\|^H \mathbf{U}'\right)}{\mathrm{norm}\left(\|C\|^H \mathbf{U}'\right)} \tag{10}$$

of the GMRES solver is important both in terms of time and accuracy. Therefore, once the unknown plane wave coefficients are determined, the near-field error

$$\epsilon = \mathrm{norm}\left(\tilde{\mathbf{J}}'_{\mathrm{final}} - \|C\|^H \mathbf{U}'\right) \tag{11}$$

is determined to compare the near field reproduced by plane wave sources with the given near field. It has been found empirically

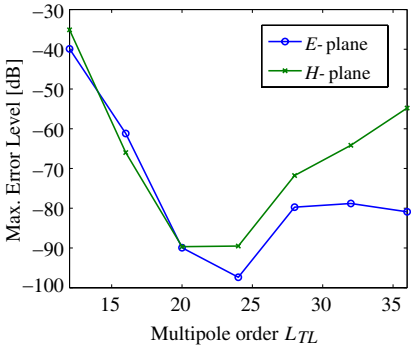

Figure 1. Multipole order L_{T_L} vs. max. error level in E- and H-plane of horn antenna.

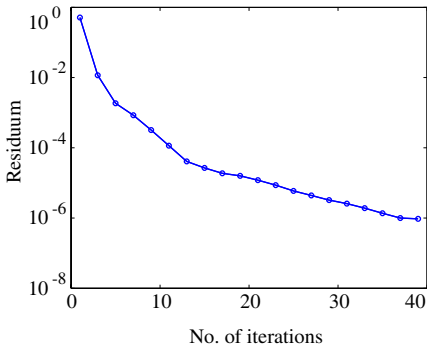

Figure 2. Relative residuum vs. No. of iterations of GMRES solver for horn antenna.

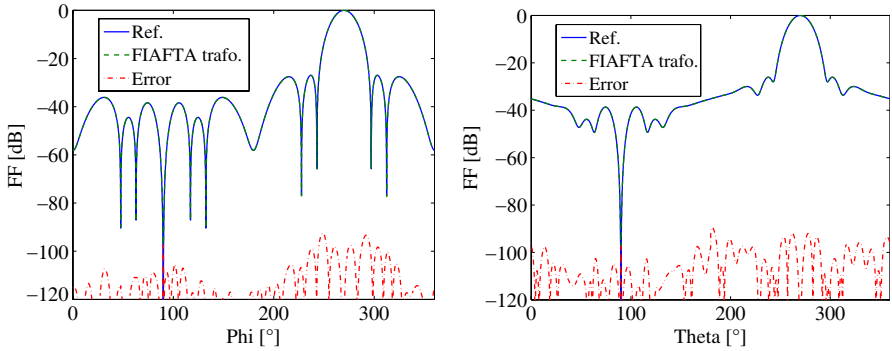

(a) E-plane pattern cut (b) H-plane pattern cut

Figure 3. Transformed E- and H-plane pattern cuts of horn antenna operating at 10 GHz.

that when the near-field error is on the order of 10^{-3} or when the difference between the residuum of the GMRES solver in consecutive two iterations tends to remain the same, the far-field error level

$$\text{Error level} = 20\log_{10}(\text{abs}\,(|\mathbf{E}_{\text{ref}}\,(\theta,\phi)\,| - |\mathbf{E}_{\text{trans}}\,(\theta,\phi)\,|)) \qquad (12)$$

is well below < -70 dB. A similar criterion was applied for the synthetic horn antenna using spherical measurements. At the 38th iteration it satisfies the above described condition. Fig. 2 shows the logarithmic decrease in the residuum of the GMRES solver versus the number of iterations. As observed, the residuum decreases rapidly in the beginning but after a certain number of iterations the rate of convergence becomes very slow and the relative residuum stays almost constant.

The transformed pattern cuts of the horn antenna using 6 hierarchical levels, 3 buffer boxes, and 10^{-4} accuracy of the multipole expansion of the translation operator are shown in Fig. 3. In the spherical setup, the AUT is looking in $-y$ direction and the whole spherical surface is considered. A near-field error ϵ of less than 10^{-4} is observed and as can be seen, the difference between the ideal and the transformed far field using FIAFTA is approaching -90 dB which can be considered negligible. The average iteration time observed is 2.1 s per iteration.

3.2. Errors Affecting Probe Output

The errors in this category are commonly known as instrumentation errors and mainly involve inaccuracies due to the RF measurement

system. These errors directly affect the magnitude and phase of the probe output. The errors include receiver amplitude and phase non-linearity, RF leakage and cross talk, random amplitude and phase error, temperature effects etc.. The degree of inaccuracy in the magnitude $\triangle a$ and the phase $\triangle\psi$ is normally provided by the receiver manufacturers. Therefore, the probe output can be written as

$$U_{\mathrm{o/p}}(\mathbf{r}_{\mathrm{M}}) = (a(\mathbf{r}_{\mathrm{M}}) + \triangle a(\mathbf{r}_{\mathrm{M}}))\, \mathrm{e}^{\mathrm{j}(\psi(\mathbf{r}_{\mathrm{M}}) + \triangle\psi(\mathbf{r}_{\mathrm{M}}))}, \tag{13}$$

where $\mathbf{r}_{\mathrm{M}}$ is the measurement point. Since the exact error magnitude is unknown, one can replace $\triangle a$ and $\triangle\psi$ by their respective standard deviations $\sigma_{\mathrm{mag}}(\mathbf{r}_{\mathrm{M}})$ and $\sigma_{\mathrm{ph}}(\mathbf{r}_{\mathrm{M}})$ according to

$$U_{\mathrm{o/p}}(\mathbf{r}_{\mathrm{M}}) = (a(\mathbf{r}_{\mathrm{M}}) + \sigma_{\mathrm{mag}}(\mathbf{r}_{\mathrm{M}}))\, \mathrm{e}^{\mathrm{j}(\psi(\mathbf{r}_{\mathrm{M}}) + \sigma_{\mathrm{ph}}(\mathbf{r}_{\mathrm{M}}))}. \tag{14}$$

The standard deviations σ_{mag} and σ_{ph} can be defined according to the corresponding instrumentation errors and its order of magnitude. For instance, we select a random error in the magnitude arising due to the noise addition by the receiver. A unique and effective way of representing the standard deviation is by considering the SNR of the measured signal as defined in [21]. The available absolute noise of the receiver is taken into account and the empirically derived SNR based standard deviation is given as

$$3\sigma_{\mathrm{mag}} = 20\log_{10}\left(1 + \sqrt{\frac{0.5}{10^{\frac{\mathrm{SNR}}{10}}}}\right). \tag{15}$$

An SNR of 60 dB produces an inaccuracy of ± 0.006 dB at normalized maximum pattern level (i.e., 0 dB) using (15). Similarly, at -30 dB normalized pattern level the inaccuracy is ± 0.2 dB. The SNR value at the maximum pattern level can be varied according to the specification of the given RF measurement setup.

The effect of any other instrumentation error can be introduced in a similar way. Once the standard deviation of the amplitude and the phase error is available, the error in the probe output U_{err} can be approximated from the available erroneous near-field data. The probe output can then be represented as $U_{\mathrm{o}} = U_{\mathrm{ef}} + U_{\mathrm{err}}$, where U_{ef} is the assumed error free near-field data. Using the linearity of the problem, the probe output

$$\mathbf{U}'_{\mathrm{o}} = -\mathrm{j}\frac{\omega\mu}{4\pi}\, \|C\| \cdot \tilde{\mathbf{J}}'_{\mathrm{o}} \tag{16}$$

can be modified as

$$\mathbf{U}'_{\mathrm{ef}} + \mathbf{U}'_{\mathrm{err}} = -\mathrm{j}\frac{\omega\mu}{4\pi}\, \|C\| \cdot \left(\tilde{\mathbf{J}}'_{\mathrm{ef}} + \tilde{\mathbf{J}}'_{\mathrm{err}}\right). \tag{17}$$

The error in the plane wave spectrum $\tilde{\mathbf{J}}'_{\mathrm{err}}$ is computed by solving

$$\mathbf{U}'_{\mathrm{err}} = -\mathrm{j}\frac{\omega\mu}{4\pi}\, \|C\| \cdot \tilde{\mathbf{J}}'_{\mathrm{err}} \tag{18}$$

and utilizing the amplitude and the phase error distributions of the near field. The normalized error spectrum $\tilde{\mathbf{J}}'^{\mathrm{n}}_{\mathrm{err}}$ is obtained by utilizing $\tilde{\mathbf{J}}'_{\mathrm{o}}$ as

$$\tilde{\mathbf{J}}'^{\mathrm{n}}_{\mathrm{err}} = \frac{\tilde{\mathbf{J}}'_{\mathrm{err}}}{\max(|\tilde{\mathbf{J}}'_{\mathrm{o}}|)}. \tag{19}$$

Since the plane wave coefficients directly represent the far field of the AUT, the estimated maximum and the mean error can be calculated as

$$E^{\mathrm{est}}_{\mathrm{max}} = \max\left(20\log\left(\left|\tilde{\mathbf{J}}'^{\mathrm{n}}_{\mathrm{err}}\right|\right)\right), \tag{20}$$

$$E^{\mathrm{est}}_{\mathrm{mean}} = \frac{\sum\left(20\log\left(\left|\tilde{\mathbf{J}}'^{\mathrm{n}}_{\mathrm{err}}\right|\right)\right)}{\text{no. of plane wave coefficients}}. \tag{21}$$

It is emphasized that the given procedure is equally valid for arbitrary near-field measurements and only requires the commonly available uncertainty in the measured probe output. The coupling matrix $\|C\|$ takes care of the plane wave translations to the measurement points of the arbitrary grid. Therefore, the estimated error in the plane wave spectrum for the same inaccuracy in the probe output can differ for different measurement surfaces.

The use of the synthetic approach allows us to compare the estimated error with that of the observed error in the plane wave spectrum. The reference plane wave spectrum $\tilde{\mathbf{J}}'_{\mathrm{ref}}$ using ideal near-field data is compared with the erroneous plane wave spectrum $\tilde{\mathbf{J}}'_{\mathrm{o}}$ and the "reference" maximum and mean error is computed as

$$E^{\mathrm{ref}}_{\mathrm{max}} = \max\left(20\log\left(\mathrm{abs}\left(\left|\tilde{\mathbf{J}}'_{\mathrm{o}}\right| - \left|\tilde{\mathbf{J}}'_{\mathrm{ref}}\right|\right)\right)\right) \tag{22}$$

$$E^{\mathrm{ref}}_{\mathrm{mean}} = \frac{\sum\left(20\log\left(\mathrm{abs}\left(\left|\tilde{\mathbf{J}}'_{\mathrm{o}}\right| - \left|\tilde{\mathbf{J}}'_{\mathrm{ref}}\right|\right)\right)\right)}{\text{no. of plane wave coefficients}}. \tag{23}$$

The directivity

$$D_{\mathrm{AUT}} = 10\log\left(\frac{4\pi}{\sum\limits_{k_\phi}\sum\limits_{k_\theta}\tilde{\mathbf{J}}'^{2}(k_\phi, k_\theta)\, W(k_\theta)}\right) \tag{24}$$

of the AUT is also computed following the same methodology and the estimated error in the directivity is computed using $\tilde{\mathbf{J}}'^{\mathrm{n}}_{\mathrm{err}}$. The reference error $D^{\mathrm{ref}}_{\mathrm{err}}$ in the directivity is obtained by subtracting D_{ref}

from D_o. The normalized plane wave spectra were used to compute the erroneous and the reference directivities. The $W(k_\theta)$ factor in (24) represents the weighting factor of the Gauss-Legendre quadrature used for the discrete representation of the spectral integral [24].

To assess the performance of the proposed error model, we superimpose randomly distributed magnitude errors (given by (15)) assuming 50 dB SNR at the normalized maximum pattern level and a phase error with a standard deviation $\sigma_{ph} = 1^\circ$ on the unperturbed near-field data of a horn antenna. Another realization but using the same standard deviation is used to compute the error in the plane wave spectrum. The observed error in the plane wave spectrum using perturbed near-field data and the estimated error using only the error distribution in the probe output for spherical measurements are then compared. The behavior is shown in Fig. 5. The analysis is extended to cylindrical and planar near-field measurements as well and the resulting error values are composed in Table 1. A square shaped planar

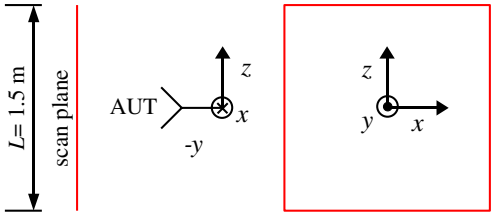

Figure 4. Planar near-field measurement setup.

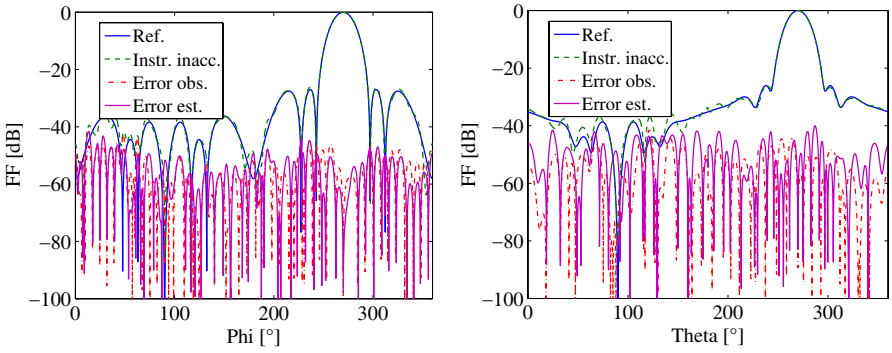

(a) E-plane pattern cut (b) H-plane pattern cut

Figure 5. Transformed E- and H-plane pattern cuts of a horn antenna using near-field data contaminated with random magnitude and phase errors.

Table 1. Far-field uncertainty [dB] in the transformed E- and H-plane pattern cuts due to random amplitude errors for a horn antenna operating at 10 GHz.

AUT	Random Errors									
	E-plane				H-plane				D_{AUT}	
	mean err		max err		mean err		max err		error	
	est.	ref.	est.	ref.	est.	ref.	est.	ref.	est.	ref.
Spherical	−57	−56	−43	−43	−56	−57	−41	−42	0.01	0.01
Cylindrical	−59	−59	−48	−49	−59	−60	−45	−45	0.01	0.01
Planar	−69	−66	−48	−44	−70	−71	−49	−52	0.00	0.00

measurement surface (xz) at $y = -0.4$ m is used to collect the near-field data, as shown in Fig. 4. The length and the width of the planar surface are 1.5 m each which makes a valid angle of 60°. Similarly, the radius and the height of the cylindrical surface used is 0.4 m and 1 m, respectively, with AUT looking in $-y$ direction and makes a valid angle of 48° in the E-plane pattern. A good agreement noticed in the estimated and the observed uncertainty in the transformed pattern clearly shows that if the magnitude of the near-field error is known, one can estimate the uncertainty in the far field very accurately.

3.3. Errors Affecting the Probe Coefficients

Probe parameter errors include errors affecting the probe correction coefficient $\mathbf{P}(.,.,.,.)$ in (4). The errors include probe pattern inaccuracy, probe polarization ratio, probe gain, and probe alignment error. Any such error directly affects the accuracy of the coupling matrix elements

$$C_{\phi/\theta}(k_{\phi p}, k_{\theta q}, \phi_m, \theta_n) = T_L\left(\hat{k}, \mathbf{r}_{\mathrm{M}}\right) W(k_{\theta q}) P\left(k_{\phi p}, k_{\theta q}, \phi_m, \theta_n\right) \quad (25)$$

and in turn deteriorates the transformed radiation pattern. The number of integration points $p = 1, \ldots, P$ and $q = 1, \ldots, Q$ in ϕ- and θ-direction, respectively, are used in the above equation. Using an analogous procedure as described in the previous section, we split the erroneous probe correction coefficient into an error free $\mathbf{P}_{\mathrm{ef}}(.,.,.,.)$ and a probe error part $\mathbf{P}_{\mathrm{err}}(.,.,.,.)$ according to

$$\begin{aligned} C_{\phi/\theta}(k_{\phi p}, k_{\theta q}, \phi_m, \theta_n) \;=\; & T_L(\hat{k}, \mathbf{r}_{\mathrm{M}}) W(k_{\theta q}) \left(P_{\mathrm{ef}}\left(k_{\phi}, k_{\theta}, \phi_m, \theta_n\right)\right. \\ & \left. + P_{\mathrm{err}}\left(k_{\phi p}, k_{\theta q}, \phi_m, \theta_n\right)\right). \end{aligned} \quad (26)$$

Accordingly, the coupling matrix elements can also be divided into two parts

$$C_{\text{ef}}(k_{\phi p}, k_{\theta q}, \phi_m, \theta_n) + C_{\text{err}}(k_{\phi p}, k_{\theta q}, \phi_m, \theta_n) = T_L(\hat{k}, \mathbf{r}_{\text{M}}) W(k_{\theta q})$$
$$(P_{\text{ef}}(k_{\phi}, k_{\theta}, \phi_m, \theta_n) + P_{\text{err}}(k_{\phi p}, k_{\theta q}, \phi_m, \theta_n)) \tag{27}$$

and the probe output is modified as

$$\mathbf{U}'_{\text{o}} = -\text{j}\frac{\omega\mu}{4\pi}\left(\|C\|_{\text{ef}} + \|C\|_{\text{err}}\right) \cdot \tilde{\mathbf{J}}'_{\text{o}}. \tag{28}$$

A known uncertainty in the probe alignment, probe pattern inaccuracies and other probe errors allow us to compute $\|C\|_{\text{err}}$ which in combination with the plane wave spectrum $\tilde{\mathbf{J}}'_{\text{o}}$, gives the uncertainty in the probe output

$$\mathbf{U}'_{\text{err}} = -\text{j}\frac{\omega\mu}{4\pi}\|C\|_{\text{err}} \cdot \tilde{\mathbf{J}}'_{\text{o}}. \tag{29}$$

Once the uncertainty in the probe output is obtained, the error in the plane wave spectrum $\tilde{\mathbf{J}}'_{\text{err}}$ can be computed using

$$\mathbf{U}'_{\text{err}} = -\text{j}\frac{\omega\mu}{4\pi}\|C\| \cdot \tilde{\mathbf{J}}'_{\text{err}}. \tag{30}$$

The directivity, estimated mean, and maximum errors can then be computed using (18), (19), and (22).

To examine the effectiveness of the given procedure, we introduce randomly generated magnitude errors in the probe pattern used for the probe correction of the horn antenna. The erroneous plane wave spectrum $\tilde{\mathbf{J}}'_{\text{o}}$ is determined using the perturbed probe pattern. The uncertainty in $\tilde{\mathbf{J}}'_{\text{o}}$ is approximated by using another randomly generated error distribution[‡] and following the above mentioned procedure. The observed and the estimated errors in the transformed E- and H-plane cuts for spherical measurements are shown in Fig. 6. The transformed pattern shows stability against magnitude errors in the probe pattern and good agreement in the observed and the estimated errors is seen. Table 2 summarizes the estimated and the reference error values for spherical, cylindrical, and planar scanning surfaces.

3.4. Errors Affecting the Translation Operators

The positioning system used in the near-field measurement system can mark the position of a measurement point with an accuracy of several

[‡] The standard deviation used to generate the error distribution, however, is the same and uses 50 dB SNR at the normalized maximum pattern level.

Table 2. Far-field uncertainty [dB] in the transformed E- and H-plane pattern cuts due to probe pattern error for a horn antenna operating at 10 GHz.

AUT	Probe Pattern Error									
	E-plane				H-plane				D_{AUT}	
	mean err		max err		mean err		max err		error	
	est.	ref.	est.	ref.	est.	ref.	est.	ref.	est.	ref.
Spherical	−100	−100	−71	−71	−98	−99	−85	−86	0.00	0.00
Cylindrical	−85	−87	−66	−67	−90	−90	−66	−66	0.00	0.00
Planar	−105	−104	−64	−66	−101	−99	−62	−63	0.00	0.00

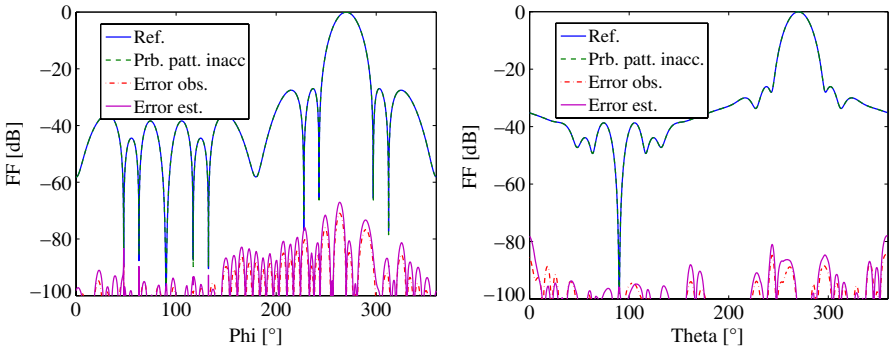

(a) E-plane pattern cut (b) H-plane pattern cut

Figure 6. Transformed E- and H-plane pattern cuts of a horn antenna using near-field data contaminated with probe pattern errors.

tens of micrometers. No matter how small the position error is, it results in an inaccurate translation of the plane wave spectrum and introduces uncertainty in the transformed pattern. The relative error in the x, y, and z coordinates, i.e., δx, δy, and δz of the probe position can be determined using optical measurements or it can be obtained from specifications of the positioner used in the measurements. We make use of the position inaccuracy to determine the uncertainty in the transformed pattern. An erroneous measurement point

$$\mathbf{r}_{\mathrm{M}} + \delta\mathbf{r}_{\mathrm{M}} = (x + \delta x)\hat{a}_x + (y + \delta y)\hat{a}_y + (z + \delta z)\hat{a}_z \tag{31}$$

is a combination of the actual measurement point $\mathbf{r}_{\mathrm{M}}$ and the inaccuracy $\delta\mathbf{r}_{\mathrm{M}}$. Consequently, the modified translation operator is

rewritten as

$$T_L\left(\hat{k}, \mathbf{r}_\mathrm{M} + \delta\mathbf{r}_\mathrm{M}\right) = -\mathrm{j}\frac{k}{4\pi}\sum_{l=0}^{L}(-\mathrm{j})^l(2l+1) \mathrm{h}_l^{(2)}\left(k\left(\mathbf{r}_\mathrm{M} + \delta\mathbf{r}_\mathrm{M}\right)\right)\mathrm{P}_l\left(\hat{k}\cdot\left(\mathbf{r}_\mathrm{M} + \delta\hat{r}_\mathrm{M}\right)\right). \quad (32)$$

It is worth mentioning here that one cannot use the error in the probe position $\delta\mathbf{r}_\mathrm{M}$ directly to compute the error in the translation operator. The inaccuracy in the translation operator

$$\delta T_{L\mathrm{err}} = T_L\left(\hat{k}, \mathbf{r}_\mathrm{M} + \triangle\mathbf{r}_\mathrm{M}\right) - T_L\left(\hat{k}, \mathbf{r}_\mathrm{M}\right) \quad (33)$$

is used to compute the erroneous coupling matrix elements

$$C_\mathrm{err}(k_{\phi p}, k_{\theta q}, \phi_m, \theta_n) = \delta T_{L\mathrm{err}} W(k_{\theta q}) P(k_{\phi p}, k_{\theta q}, \phi_m, \theta_n). \quad (34)$$

The error in the probe output

$$\mathbf{U}'_\mathrm{err} = -\mathrm{j}\frac{\omega\mu}{4\pi}\|C\|_\mathrm{err}\cdot\tilde{\mathbf{J}}'_\mathrm{o} \quad (35)$$

and the error in the plane wave spectrum

$$\mathbf{U}'_\mathrm{err} = -\mathrm{j}\frac{\omega\mu}{4\pi}\|C\|\cdot\tilde{\mathbf{J}}'_\mathrm{err} \quad (36)$$

are used along with (18), (19), and (22) to compute the estimated mean and maximum errors.

The behavior of FIAFTA against probe positioning errors is analyzed by adding randomly distributed errors in the probe coordinates. A realistic standard deviation in the probe coordinates

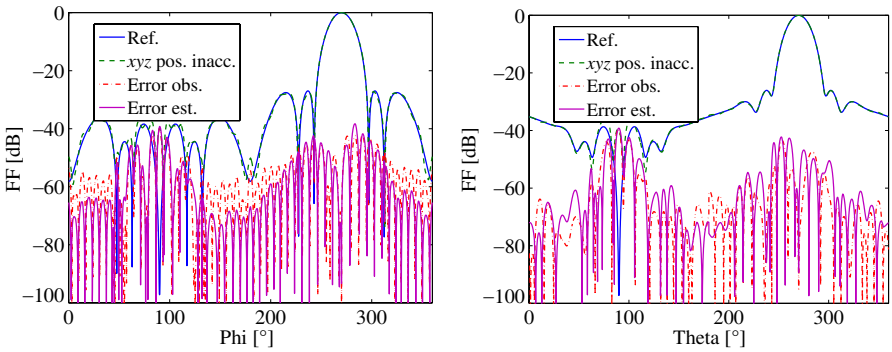

(a) *E*-plane pattern cut (b) *H*-plane pattern cut

Figure 7. Transformed *E*- and *H*-plane pattern cuts for the horn antenna incorporating probe position inaccuracies.

Table 3. Far-field uncertainties [dB] in the transformed E- and H-plane pattern cuts due to probe position errors for the horn antenna operating at 10 GHz.

AUT	Probe Position Error									
	E-plane				H-plane				D_{AUT}	
	mean err		max err		mean err		max err		err	
	est.	ref.	est.	ref.	est.	ref.	est.	ref.	est.	ref.
Spherical	−61	−54	−43	−42	−64	−64	−43	−43	0.01	0.02
Cylindrical	−70	−68	−49	−53	−58	−59	−36	−43	0.00	0.00
Planar	−70	−70	−52	−48	−70	−74	−53	−52	0.01	0.00

$\sigma_x = \sigma_y = \sigma_z = 50\,\mu\mathrm{m}$ is chosen and the resulting error in the transformed pattern is compared with the estimated mean and maximum errors. The transformed E- and H-plane pattern cuts of the horn antenna with the observed and estimated errors for spherical measurements are shown in Fig. 7. The analysis is also extended for the cylindrical and planar scanning surfaces and the error values are summarized in Table 3. Again a good agreement in the estimated and the reference error values is seen.

The schematic summarizing the analysis for the instrumentation, probe parameter, and the probe positioning errors is shown in Fig. 8. By following the mentioned steps one can estimate the maximum and the mean uncertainty in the transformed far-field pattern.

3.5. General Errors

The errors falling in this category do not directly affect the probe output, probe coefficient, or the translation operator but have an inherent effect on the near-field measurements. In the following, we discuss these errors with their effect on the transformed pattern along with any correction technique available.

3.5.1. Scan Area Truncation

Scan area truncation is one of the unavoidable sources of error in planar and cylindrical near-field measurements. The inability to measure the near field on a surface with infinite extent results in limiting the radiation behavior of the AUT to a certain reliable region. The assumption of zero near field outside the scan area incorporates errors within the valid region as well. However, the behavior of FIAFTA

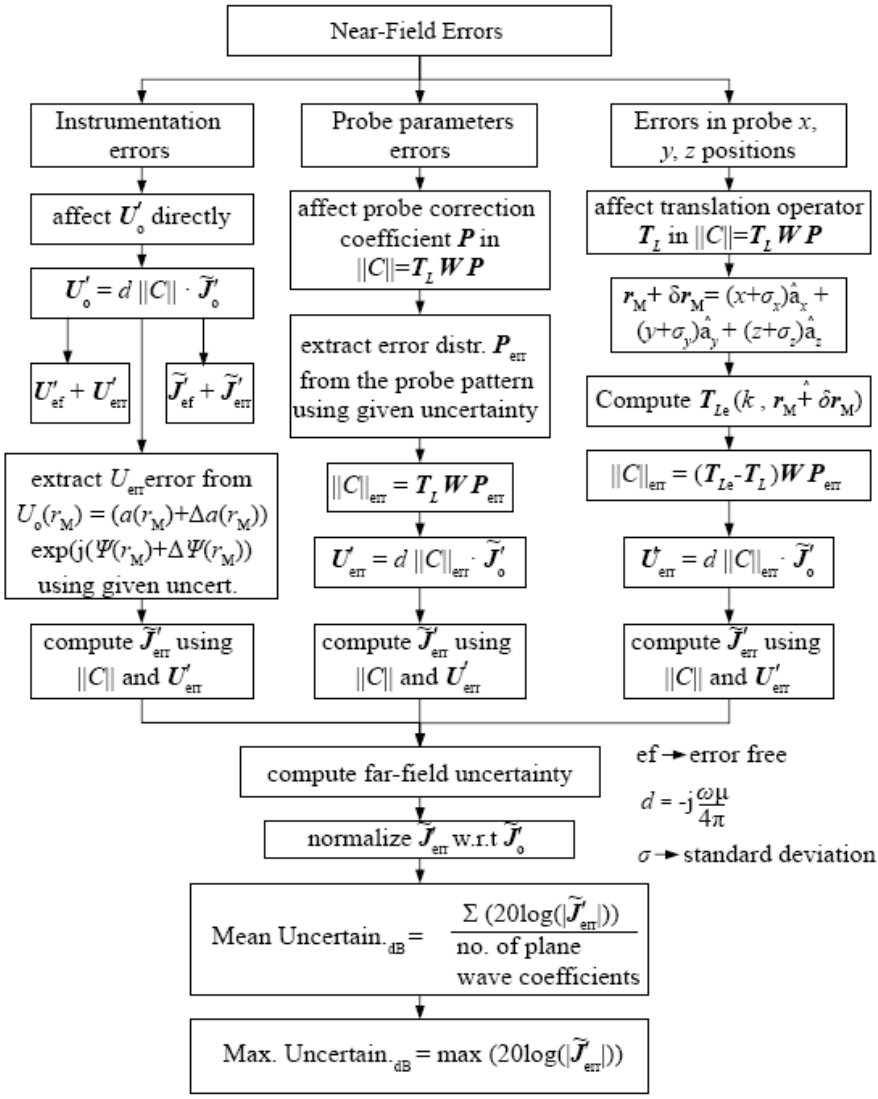

Figure 8. Schematic of the near-field measurement error analysis.

against scan area truncation is found more robust [20] as compared to the traditional transformation techniques. The better performance comes from the fact that, unlike other plane wave based approaches, FIAFTA uses the entire Ewald sphere for the representation of the

plane wave sources. Also, FIAFTA first transforms the measured data to the source plane to determine the coefficients for equivalent sources from which the far field is ascertained. The use of complete Ewald sphere and the fact that FIAFTA does not transform the measured data in the first step helps in reducing the truncation error [31] and avoids ripples in the far-field pattern. The ripples can also be eliminated by using direct non-redundant NFFF transformation in a cylindrical scanning geometry proposed by D'Agostino et al. in [32]. The overall effect of scan area truncation can be assumed negligible if the truncation level at the edges of the scan plane is $\leq -40\,\mathrm{dB}$. Since FIAFTA can handle measurements on arbitrary grids, the valid angle of the radiation pattern can be significantly increased by utilizing adaptive sampling in planar and cylindrical measurements [33, 34].

3.5.2. Data Point Spacing

The spacing between sample points on the near-field scanning surface greatly affects the accuracy of the transformed far field. $\lambda/2$ sample spacing is commonly adopted along the length of the cylinder in the standard cylindrical and in the planar measurements due to FFT usage. Sample spacings coarser than $\lambda/2$ result in aliasing errors [5]. However, no such limitation applies to FIAFTA and the sample spacing is computed in relation with the number of unknowns required to solve the linear system of equations. The required spacing in θ and ϕ is

$$\triangle\phi = \pi/(\alpha_1 L_{\mathrm{AUT}}) \tag{37}$$

$$\triangle\theta = \pi/\left(\alpha_2 L_{\mathrm{AUT}} - 1^{\S}\right) \tag{38}$$

where α_1 and α_2 are the proportionality constants with empirical values slightly greater than $1^{\|}$ and $L_{\mathrm{AUT}} = kd_a/2{+}10$ is the antenna multipole number with d_a as the diameter of the minimum sphere enclosing the antenna. Once the spacing in θ and ϕ is determined, the samples are efficiently distributed on the spherical surface and can then be mapped to planar [35], cylindrical, or any arbitrary surface. As long as the given sampling criteria are satisfied, negligible errors in the transformed pattern are observed.

3.5.3. Multiple Reflections

It is common practice to place the scan plane near the AUT so that the valid angle can be efficiently increased. Nonetheless, it

§ To include samples at the poles, a constant value "1" is subtracted from the number of measurement points in θ.

‖ The optimum value of α_1 and α_2 depends on the noise conditions and other systematic errors.

results in strong interactions between the AUT and the probe and the resulting multiple reflections deteriorate the measured data especially for planar measurements. Yaghjian tried to establish the upper bound due to multiple reflection errors [4] which predicts very large errors. Estimating multiple reflection errors is extremely difficult as it varies according to the choice of the probe and the separation between the AUT and the probe. A commonly employed method to reduce multiple reflection errors is to perform a set of measurements on several measurement planes separated by $\lambda/2$ [5]. This practice, however, increases the measurement time significantly. The ability of FIAFTA to handle measurement data on arbitrary grids enables us to efficiently reduce the effect of multiple reflection errors by taking measurements on two partial planes [23]. The central near-field data is collected on a plane at a large distance while another plane at smaller distance is used to collect the near field from the boundary regions. In this way, one can reduce the effect of multiple reflection errors while keeping a larger valid angle and with less time consumption. The concept is validated in [23] for planar measurements and is equally applicable for cylindrical measurements (see Fig. 9). The length L_1 of the outer cylinder can be determined in a similar fashion as described in [23] and is given as

$$L_1 = \frac{1}{r}(xr_1(a-1) + ar) \tag{39}$$

where r_1 and r are the radius of the outer and the inner cylinder, respectively.

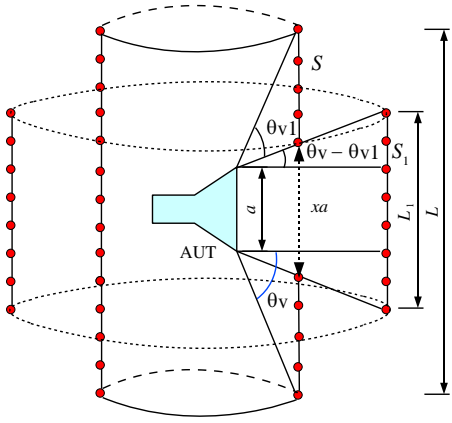

Figure 9. Schematic of near-field measurements on two partial cylindrical surfaces for reduced multiple reflection errors.

3.5.4. Room Scattering

The near-field probe receives direct as well as multipath signals scattered from different objects. The effect on the measured near field is more pronounced if the measurements are performed in a semi-anechoic chamber. However, FIAFTA has the ability to alienate the contributions of the multipath signals by attributing the echo contributions to scattering centres with or without the knowledge of the location of echo sources [36]. The modified linear system of equations is

$$\mathbf{U}' = -j\frac{\omega\mu}{4\pi}\|C\|_{\mathrm{AUT}} \cdot \tilde{\mathbf{J}} - j\frac{\omega\mu}{4\pi}\sum_{i=1}^{N_{\mathrm{SC}}}\|C\|_{\mathrm{SC}i} \cdot \tilde{\mathbf{J}}_{\mathrm{SC}i} \tag{40}$$

where $\|C\|_{\mathrm{SC}i}$ represents the coupling matrix for the i-th scattering center and N_{SC} is the number of scattering centres employed. Significant improvement have been reported in comparison to the case where no echo suppression is applied [36]. The NFFF transformations based on the nonredundant representation of electromagnetic field also allow to cut away the echo contributions outside the antenna spatial bandwidth, due to the low pass filtering properties of the employed interpolation functions, as stated in [37].

4. CONCLUSION

Arbitrary near-field errors have been analyzed for the Fast Irregular Antenna Field Transformation Algorithm (FIAFTA). The mean and the maximum errors in the transformed far field were estimated by deriving appropriate equations. The major sources of errors have been discussed and it was shown that the error model is equally suitable for all kind of antennas and is valid for arbitrary scanning geometries. Good agreement has been observed in the estimated and the observed errors in the transformed field of a synthetically modelled horn like antenna.

REFERENCES

1. Yaghjian, A. D., "An overview of near-field antenna measurements," *IEEE Trans. Antennas Propag.*, Vol. 34, No. 1, 30–45, 1986.
2. Rodrigue, G. P., E. B. Joy, and C. P. Burns, "An investigation of the accuracy of far-field radiation patterns determined from near-field measurements," Report, Georgia Institute of Technology, Atlanta, Georgia, 1973.

3. Newell, A. C. and M. L. Crawford, "Planar near-field measurements on high performance array antennas," NBSIR 74-380, National Bureau of Standards, 1974.
4. Yaghjian, A. D., "Upper-bound errors in far-field antenna parameters determined from planar near-field measurements, Part 1: Analysis," Technical Note 667, National Bureau of Standards, 1975.
5. Newell, A. C., "Error analysis techniques for planar near-field measurements," *IEEE Trans. Antennas Propag.*, Vol. 36, No. 6, 754–768, 1988.
6. Joy, E. B., "Near-field range qualification methodology," *IEEE Trans. Antennas Propag.*, Vol. 36, No. 6, 836–844, 1988.
7. Hansen, J., *Spherical Near-field Antenna Measurements*, IEEE Electromagnetic Wave Series 26, UK, 1988.
8. Bucci, O. M., G. Schirinzi, and G. Leone, "A compensation technique for probe positioning error in planar near-field measurements," *IEEE Trans. Antennas Propag.*, Vol. 36, No. 8, 1167–1172, 1988.
9. Muth, L. A. and R. L. Lewis, "A general technique to correct probe position errors in planar near-field measurements to arbitrary accuracy," *IEEE Trans. Antennas Propag.*, Vol. 38, No. 12, 1925–1932, 1990.
10. D'Agostino, F., F. Ferrara, C. Gennarelli, R. Guerriero, and M. Migliozzi, "On the compensation of probe positioning errors when using a nonredundant cylindrical Nf-Ff transformation," *Progress In Electromagnetic Research B*, Vol. 20, 321–335, 2010.
11. Newell, A. C. and C. F. Stubenrauch, "Effect of random errors in planar near-field measurements," *IEEE Trans. Antennas Propag.*, Vol. 36, No. 6, 769–773, 1988.
12. Bucci, O. M. and M. D. Migliore, "A new method for avoiding the truncation error in near-field measurements," *IEEE Trans. Antennas Propag.*, Vol. 54, No. 10, 2940–2952, 2006.
13. D'Agostino, F., F. Ferrara, C. Gennarelli, R. Guerriero, and G. Riccio, "An effective technique for reducing the truncation error in the near-field-far-field transformation with plane-polar scanning," *Progress In Electromagnetic Research*, Vol. 73, 213–238, 2007.
14. Ding, Y., Y. Lin, F. De-min, and L. Q. Zhong, "Analysis and simulation of system phase errors in planar near-field measurements on ultra-low sidelobe antennas," *Proceedings of 2010 IEEE International Conference on Ultra-wideband*, Nanjing,

China, 2010.

15. Cano-Fácila, F. J., S. Burgos, and M. Sierra-Castañer, "New methods to reduce leakage errors in planar near-field measurements," *5th European Conference on Antenna and Propagation*, Rome, Italy, 2011.
16. Schmidt, C. H., M. M. Leibfritz, and T. F. Eibert, "Fully probe corrected near-field far-field transformation employing plane wave expansion and diagonal translation operators," *IEEE Trans. Antennas Propag.*, Vol. 56, No. 3, 737–746, 2008.
17. Schmidt, C. H. and T. F. Eibert, "Multilevel plane wave based near-field far-field transformation for electrically large antennas in free-space or above material halfspace," *IEEE Trans. Antennas Propag.*, Vol. 57, No. 5, 1382–1390, 2009.
18. Nearfield Systems Inc., http://www.nearfield.com.
19. Rohde & Schwarz, http://www2.rohde-schwarz.com.
20. Qureshi, M. A., C. H. Schmidt, and T. F. Eibert, "Planar near-field measurement error analysis for multilevel plane wave based near-field far-field transformation," *33rd Annual AMTA Symposium*, Denver, CO, 2011.
21. Qureshi, M. A., C. H. Schmidt, and T. F. Eibert, "Far-field uncertainty due to instrumentation errors in multilevel plane wave based near-field far-field transformed planar near-field measurements," *6th European Conference on Antenna and Propagation*, Prague, Czech, 2012.
22. Qureshi, M. A., C. H. Schmidt, and T. F. Eibert, "Probe pattern inaccuracy in multilevel plane wave based near-field far-field transformed planar near-field measurements," *IEEE International Symposium on Antennas and Propagation*, Chicago, IL, 2012.
23. Qureshi, M. A., C. H. Schmidt, and T. F. Eibert, "Comparative probe parameter error analysis for planar near-field measurements with a novel approach for reduced probe-AUT interaction," *34th Annual AMTA Symposium*, Bellevue, WA, 2012.
24. Coifman, R., V. Rokhlin, and S. Wandzura, "The fast multipole method for the wave-equation: A pedestrian prescription," *IEEE Antennas Propag. Mag.*, Vol. 35, No. 3, 7–12, 1993.
25. Wen, J., J. Hu, and Z. P. Nie, "A novel strategy of the multipole numbers of the MLFMA," *Proc. APMC Conf.*, Vol. 3, Dec. 2005.
26. Chew, W., J. Jin, E. Michielssen, and J. Song, *Fast and Efficient Algorithms in Computational Electromagnetics*, Artech House, Boston, MA, 2001.
27. Saad, Y., *Iterative Methods for Sparse Linear Systems*, 2nd

Edition, Society of Industrial and Applied Mathematics, 2003.

28. Björck, A., *Numerical Methods for Least Squares Problems*, SIAM, Philadelphia, PA, 1996.
29. Schmidt, C. H., D. T. Schobert, and T. F. Eibert, "Electric dipole based synthetic data generation for probe-corrected near-field measurements," *5th European Conference on Antenna and Propagation*, Rome, Italy, 2011.
30. Schmidt, C. H., M. A. Qureshi, and T. F. Eibert, "Plane wave based near-field far-field transformation with adaptive field translations," *URSI General Assembly and Scientific Symposium of International Union of Radio Science*, Istanbul, Turkey, 2011.
31. Petre, P. and T. K. Sarkar, "Differences between modal expansion and integral equation methods for planar near-field to far-field transformation," *Journal of Electromagnetic Waves and Applications*, Vol. 10, No. 12, 269–271, 1996.
32. D'Agostino, F., F. Ferrara, C. Gennarelli, G. Gennarelli, R. Guerriero, and M. Migliozzi, "On the direct non-redundant near-field-to-far-field transformation in a cylindrical scanning geometry," *IEEE Antennas and Propagation Magazine*, Vol. 54, No. 1, 130–138, 2012.
33. Qureshi, M. A., C. H. Schmidt, and T. F. Eibert, "Adaptive sampling in multilevel plane wave based near-field far-field transformed planar near-field measurements," *Progress In Electromagnetics Research*, Vol. 126, 481–497, 2012.
34. Qureshi, M. A., C. H. Schmidt, and T. F. Eibert, "Adaptive sampling in cylindrical and spherical near-field antenna measurements," *34th Annual AMTA Symposium*, Bellevue, WA, 2012.
35. Qureshi, M. A., C. H. Schmidt, and T. F. Eibert, "An effective non-redundant sampling representation for planar near-field antenna measurements," *34th ESA Antenna Workshop*, Noordwijk, Netherlands, 2012.
36. Yinusa, K. A., C. H. Schmidt, and T. F. Eibert, "Modeling of unknown echoic measurement facilities with equivalent scattering centers," *6th European Conference on Antenna and Propagation*, Prague, Czech, 2012.
37. Bucci, O. M. and C. Gennarelli, "Application of nonredundant sampling representations of electromagnetic fields to NFFF transformation techniques," *International Journal of Antennas and Propagation*, Vol. 2012, ID: 319856, 2012.